LETTER

doi:10.1038/nature11321

Activity in motor–sensory projections reveals distributed coding in somatosensation

Leopoldo Petreanu[1]†, Diego A. Gutnisky[1], Daniel Huber[1]†, Ning-long Xu[1], Dan H. O'Connor[1], Lin Tian[1]†, Loren Looger[1] & Karel Svoboda[1]

Cortical-feedback projections to primary sensory areas terminate most heavily in layer 1 (L1) of the neocortex [1,2], where they make synapses with tuft dendrites of pyramidal neurons. L1 input is thought to provide 'contextual' information[3], but the signals transmitted by L1 feedback remain uncharacterized. In the rodent somatosensory system, the spatially diffuse[4] feedback projection from vibrissal motor cortex (vM1) to vibrissal somatosensory cortex (vS1, also known as the barrel cortex) may allow whisker touch to be interpreted in the context of whisker position to compute object location[5,6]. When mice palpate objects with their whiskers to localize object features[7,8], whisker touch excites vS1[9] and later vM1 in a somatotopic manner[10–13]. Here we use axonal calcium imaging to track activity in vM1→vS1 afferents in L1 of the barrel cortex while mice performed whisker-dependent object localization. Spatially intermingled individual axons represent whisker movements, touch and other behavioural features. In a subpopulation of axons, activity depends on object location and persists for seconds after touch. Neurons in the barrel cortex thus have information to integrate movements and touches of multiple whiskers over time, key components of object identification and navigation by active touch.

We trained head-fixed mice to perform a whisker-based object-localization task under a two-photon microscope with one whisker row (C row) (Fig. 1a)[12]. In each trial, a pole was moved into one of several locations within reach of the whiskers (sampling period, approximately 1 s; Supplementary Fig. 1a), arranged along the anterior–posterior axis on one side of the head (Fig. 1b). Mice moved their whiskers to determine whether the pole was either in one of several 'go' locations or in a 'no-go' location. Automated whisker tracking[14] measured whisker movements and shape. The force acting on the follicles, which underlies object localization[8,15,16], can be estimated from whisker shape changes induced by touch. A change in curvature at point p of the whisker is proportional to the force applied by the pole on the whisker[16]: $F \propto \Delta\kappa_p\ y_p$, where y_p is the bending stiffness at p. We thus present forces acting on the whiskers as the change in curvature, $\Delta\kappa$ (Supplementary Fig. 1b). Mice report their decision about object location with licking. Imaging was performed in trained mice (descriminability (d') average,

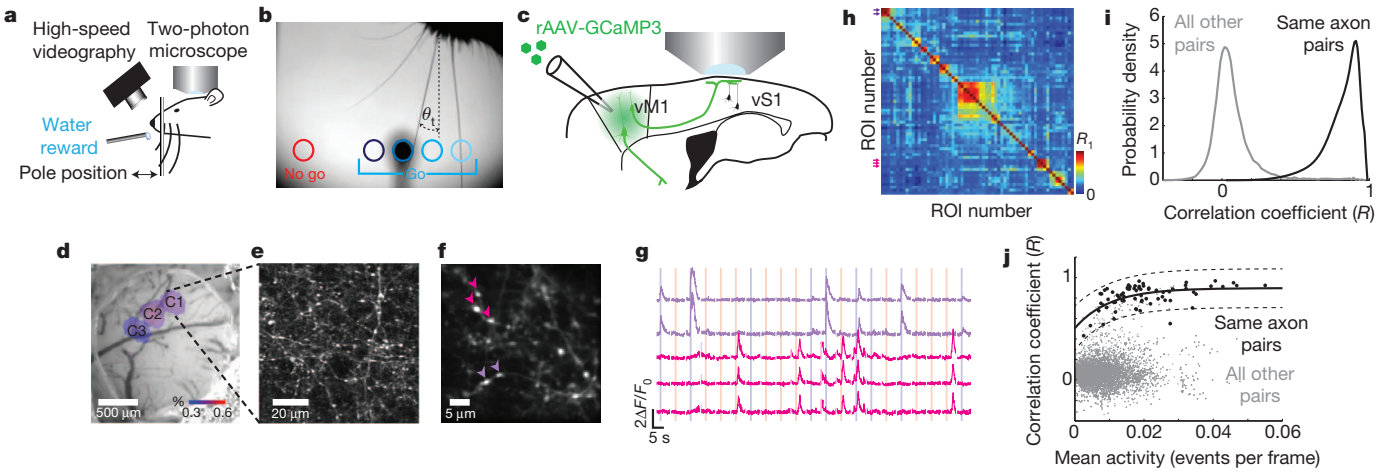

Figure 1 | Imaging activity in vM1→vS1 axons during whisker-based object localization. **a**, Head-fixed mouse performing an object-localization task under the microscope. **b**, One frame of a high-speed video sequence and typical pole positions corresponding to multiple go locations (hues of blue) and a single no-go location (red). Whisker touch was possible for all object locations for the long posterior whiskers. The azimuthal angle θ describes whisker position (θ_t denotes azimuthal angle at first touch). **c**, vM1 neurons were infected with GCaMP3-expressing virus and their axons were imaged in L1 of vS1. **d**, Intrinsic optical-imaging signals corresponding to deflections of whiskers C1, C2 and C3, overlaid on a brightfield image of the vasculature. **e**, Two-photon images showing vM1 axons in the C1 barrel column. **f**, Field of view used for *in vivo* imaging showing varicosities (arrowheads correspond to varicosities used for fluorescence time series in **g**). **g**, Fluorescence dynamics over multiple behavioural trials. Coloured bars indicate the sampling period, when the pole is within reach (blue, go trials; red, no-go trials). **h**, Matrix of correlation coefficients for activity in different varicosities in one field of view. Arrowheads correspond to varicosities marked in **f**. **i**, Distribution of correlation coefficients for all fields of view. Black line denotes pairs of varicosities on the same axon (78 varicosities, 31 axons) and grey line denotes all other varicosity pairs (51,325 varicosities). Correlation coefficients were computed over the entire session. **j**, Correlation coefficients as a function of mean activity level (black denotes pairs of varicosities on the same axon and grey denotes all other pairs). The solid line is an exponential fit ($y = a(1 - e^{-bx}) + c$) to the black circles and the dashed lines represent the 95% confidence interval.

[1]Janelia Farm Research Campus, Howard Hughes Medical Institute, Ashburn, Virginia 20147, USA. †Present addresses: Department for Basic Neurosciences, University of Geneva, Geneva CH-1211, Switzerland (D.H.); Champalimaud Neuroscience Programme, Lisbon 1400-038, Portugal (L.P.); Department of Biochemistry and Molecular Medicine. School of Medicine, University of California, Davis California 95616, USA (L.T.).

1.8, corresponding to 80% correct trials; range, 1.2–2.6) (Supplementary Fig. 1c–e).

To image activity in vM1→vS1 axons we expressed the genetically encoded calcium indicator GCaMP3 (ref. 17) in vM1 neurons[5,12] and implanted a chronic imaging window over vS1 (ref. 18) (Fig. 1c). Imaging was in barrel columns with principal whiskers C1, C2 or C3, based on intrinsic signal imaging[19] (Fig. 1d). Fluorescent axons were abundant in L1 (Fig. 1e, f and Supplementary Fig. 2a, b). GCaMP3-positive axonal varicosities appeared as bright spots along the axon backbone[20]. Two-photon time-lapse images (field of view, 40 μm × 40 μm) were acquired using raster scanning (16 Hz) over 100–200 trials per imaging location (trial duration, 7 s) (Fig. 1f, g and Supplementary Fig. 1c, d).

Action potentials reliably invade cortical axonal arborizations and cause calcium accumulations in varicosities[21], which harbour synaptic terminals. We measured GCaMP3-mediated fluorescence transients, corresponding to trains of action potentials (≥5; Supplementary Fig. 2c–f), in regions of interest (ROIs) containing individual varicosities (range, 35–80 varicosities per field of view; 17 fields of view; 6 mice). Fluorescence transients were detected in multiple ROIs within each field of view (range, 6–20 active varicosities per field of view) (Figs 1f and 2a). As expected, the fluorescence signals from varicosities belonging to the same axon were highly correlated, whereas correlations computed across all other pairs were low (Fig. 1g). These correlations allowed us to identify varicosities on the same axon, even in cases where the local arborization could not be reconstructed morphologically (Fig. 1h–j). Below we report the activity of one varicosity per axon to represent the activity of the entire axon. Only active axons were analysed (Methods). This ensured that almost all (>99%) fluorescence signals reported neural activity rather than movement (Supplementary Fig. 3).

We aligned fluorescence time series with recordings of behavioural features, including $\Delta\kappa$, whisker movements (whisking) and lick rate, and grouped trials by trial type (Fig. 2). Axonal activity was concentrated around the sampling period, and correlated with specific behavioural variables. Some axons were active coincident with whisking before and during the sampling period (Fig. 2b–d; compare ROI1 and whisking amplitude), whereas other axons were mainly active in trials with strong whisker touch (compare ROI2 and $\Delta\kappa$). Some axons were primarily active during licking or could not obviously be explained by a single behavioural feature[12]. Correlations between activity and behaviour were apparent across trials and within trials. These data indicate that individual vM1→vS1 axons represent specific behavioural features, but the representations are diverse across the population of axons.

We used a generalized form of regression (Random Forests, Methods) to quantify how behavioural features are represented by vM1→vS1 axons[12]. Both behaviour and activity varied within trials, across individual trials and across trial types (Fig. 2b, c). For example, in some trials whisker touch was strong, whereas in other trials it was weak or absent (touch in no-go trials was typically the weakest; Supplementary Fig. 1b, e). In some trials mice whisked gingerly and late during the sampling period (Fig. 2b, trial 144), whereas in other trials they whipped their whiskers against the pole as soon as it came within reach (Fig. 2b, trial 145). Our algorithms exploit this variability and the large number of trials in our data set (Supplementary Fig. 1d)

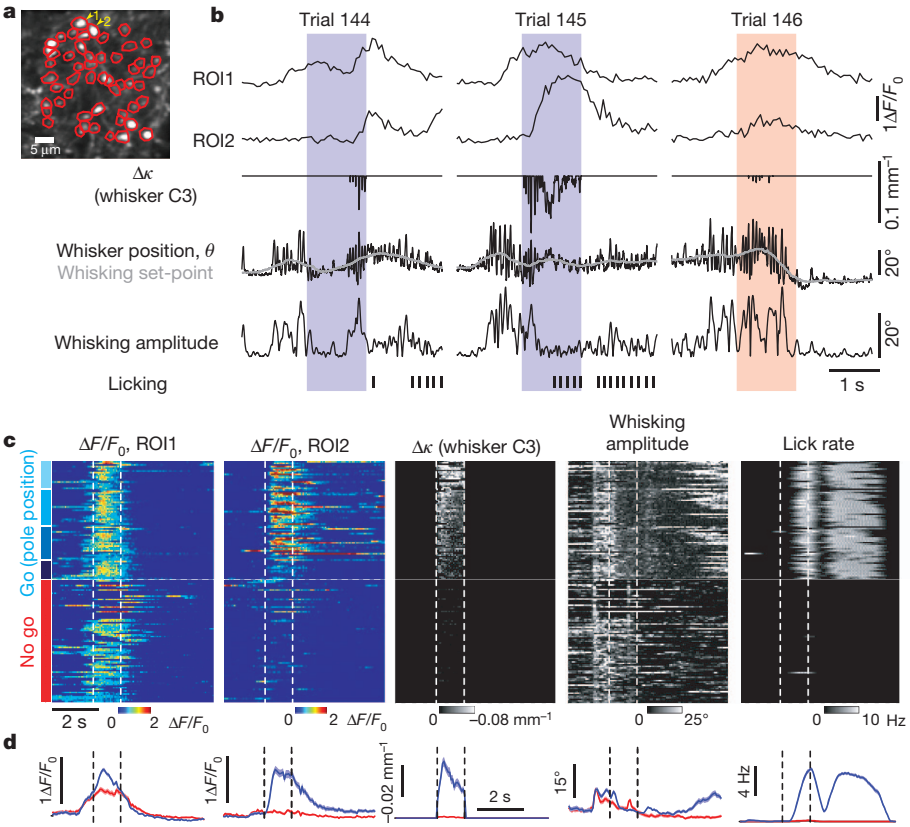

Figure 2 | Motor and sensory signals in vM1→vS1 axons. **a**, Image of the field of view and ROIs (red) corresponding to all visible axonal varicosities. Yellow numbers indicate ROI1 and ROI2. **b**, Activity ($\Delta F/F_0$) of two individual axons (ROI1 and ROI2) across three trials of one behavioural session, aligned with different behavioural features (whisker position, whisking set-point, whisking amplitude, $\Delta\kappa$, licking (ticks)). Protraction forces correspond to negative $\Delta\kappa$. Coloured bars indicate the sampling period (blue, go trials; red, no-go trials). **c**, Activity across an entire session for two axons ($\Delta F/F_0$ ROI1; $\Delta F/F_0$ ROI2). Each row corresponds to a trial. Dashed white lines indicate the sampling period when the pole is within reach. Trial type is indicated on the far left (hues of blue correspond to different object locations in go trials, as indicated in Fig. 1b). Only correct trials are shown. Right, behavioural variables (see Methods). $\Delta\kappa$ due to protractions; retractions are not shown. Whisking amplitude is the amplitude of the band-pass filtered (6–30 Hz) whisker angle. Lick rate is the instantaneous rate of tongue protractions. **d**, Activity (left) and behavioural variables (right) averaged across trial types. Shading represents s.e.m.

to quantify how well specific behavioural features could be decoded from axonal activity.

We first decoded the measured behavioural features ($\Delta\kappa$; whisking and licking; Methods) on the basis of activity in all axons in a field of view (Fig. 3a). The algorithms used the activity of populations of axons to fit individual behavioural features, taking into account variability within and across trials. The explained variance (R_i^2, for the ith behavioural feature) was used to measure the quality of decoding (Supplementary Fig. 4).

Population activity decoded the recorded behavioural features, including $\Delta\kappa$, whisking and lick rate (Fig. 3a). Whisking was decomposed into set-point (<1.6 Hz) and amplitude (6–30 Hz; Methods)[6,12] (Fig. 2b), but these parameters were highly correlated (Supplementary Fig. 5a) and decoding was similar for these parameters. All imaged fields of view decoded all behavioural features (R^2 larger than for trial-shuffled data; $P < 0.001$, bootstrap test for all sessions and features (Supplementary Fig. 4a)). This is despite the fact that each experiment sampled only approximately 1×10^{-5}% of the synapses in vS1 (assuming: thickness of L1 in vS1, 0.09 mm (ref. 22); vS1 area, 2 mm^2; synaptic density, 1×10^9 per mm (refs 3 and 23)). We conclude that vM1→vS1 axons relay signals related to touch, whisking, licking and other task-related variables to vS1 in a distributed and highly redundant manner.

We used similar methods to classify individual axons on the basis of their activity patterns[12] (Methods; Fig. 3b–e). One half of the active axons (78 out of 138 active axons; 56%) decoded one or more of the

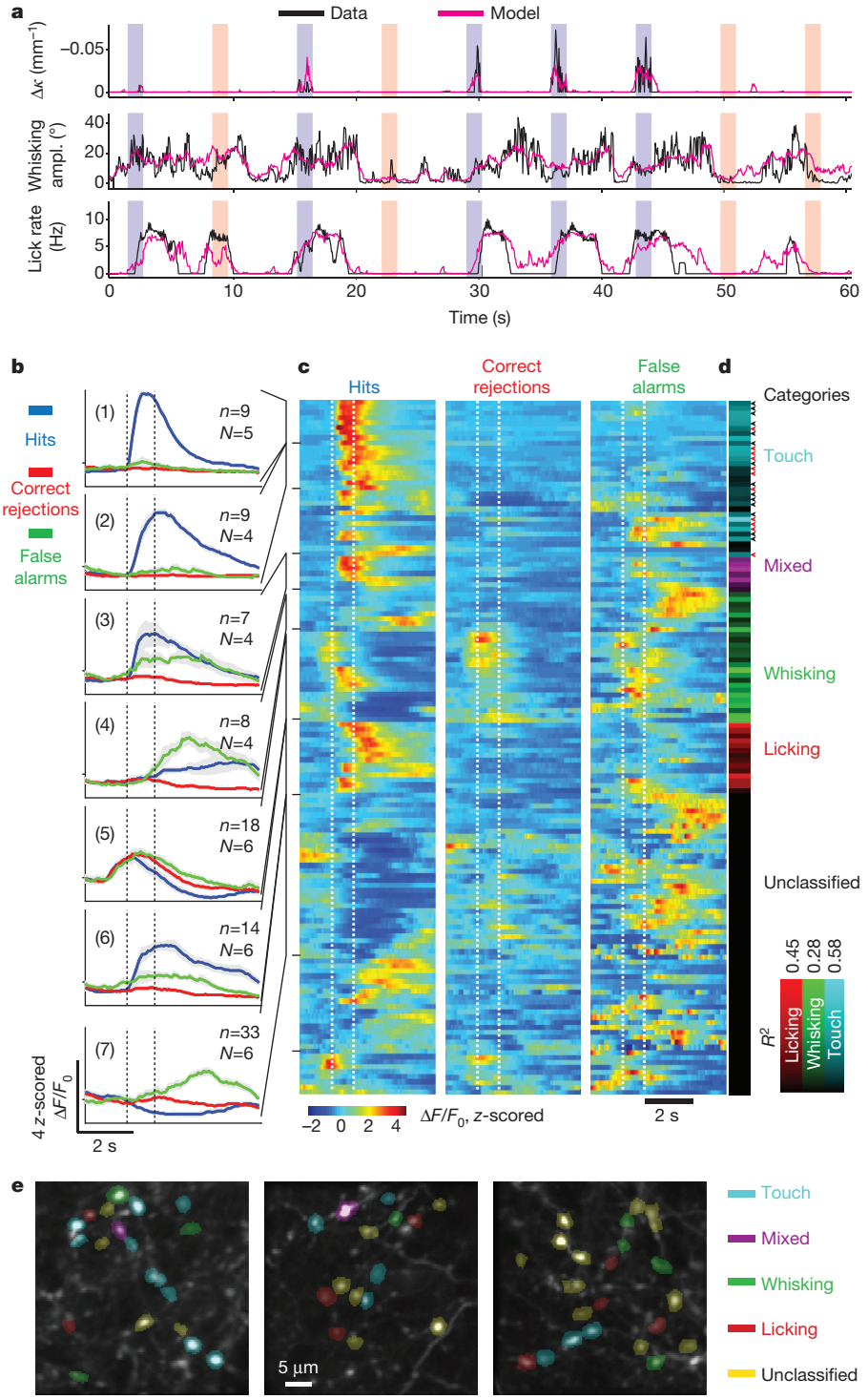

Figure 3 | Decoding behavioural variables on the basis of axonal activity. **a**, Decoding on the basis of axon populations. Time series of behavioural features down-sampled to 16 Hz (black) and the Random Forests model prediction (pink) based on the activity of all axons in one field of view. Vertical bars indicate the sampling periods and the trial type. Top, $\Delta\kappa$ induced by touch during protractions (whisker C2), a measure of contact force. Centre, whisking amplitude. Bottom, lick rate. **b**–**e**, Decoding behavioural features on the basis of the activity of individual axons. Axons were classified based on correlations with behavioural features (138 axons, 6 animals, 17 sessions). **b**, Peristimulus time histograms averaged across axons with shared activity patterns and trial types, in standardized units (z-score). Hits (blue) are correct go trials, correct rejections (red) are correct no-go trials, and false alarms (green) are incorrect no-go trials. Incorrect go trials were rare and are not shown. Correct trials and error trials were used separately in classification. N, number of animals; n, number of axons. 1, touch axons; 2, touch axons with persistent activity; 3, mixed axons; 4, whisking axons, late activity; 5, whisking axons, early activity; 6, licking axons; 7, axons that are selectively active during false alarms; these were unclassified using the behavioural features used. Grey shading represents s.e.m. **c**, Rows correspond to axons. Task-aligned activity was averaged over trials of each type. Rows were ordered on the basis of clustering by activity pattern (Methods). **d**, Correlation between the Random Forests model and different behavioural features (R_i^2) after classification (Methods). The hue indicates the strongest correlation with one of the features (cyan, touch; magenta, mixed; green, whisking; red, licking). Black and red arrowheads indicate axons showing object-location-dependent activity. Red arrowheads indicate significantly persistent axons (Fig. 4). **e**, Axons decoding different behavioural features were spatially intermingled (three sessions from three different animals). Left panel, same axons as in Fig. 2a; right panel, same axons as in Fig. 1f.

measured behavioural features (mean R^2 for best feature, 0.22). Whisking-related axons (26 out of 138 active axons) were active during whisking for all trial types, independent of touch (Fig. 2; ROI1). Whisking-related fluorescence signals lagged whisking onset (mean ± s.d., 259 ± 101 ms) (Supplementary Fig. 5b–d). However, because of the slow dynamics of calcium-dependent fluorescence we cannot exclude the possibility that the underlying spikes might lead whisking. Coding of whisking amplitude and whisking set-point is consistent with neurophysiological[6,24] and imaging experiments in vM1 (ref. 12). Touch-related axons (31 out of 138 active axons) were activated mainly in trials with touch, but not by whisking alone (Fig. 4b; Supplementary Fig. 4c). Consistently, trimming whiskers, which precluded touch during whisking, abolished activity of touch-related axons (Supplementary Fig. 6). Other axons decoded lick rate (classified as lick related)[25] or a mixture of features (classified as 'mixed' axons) (Fig. 3d).

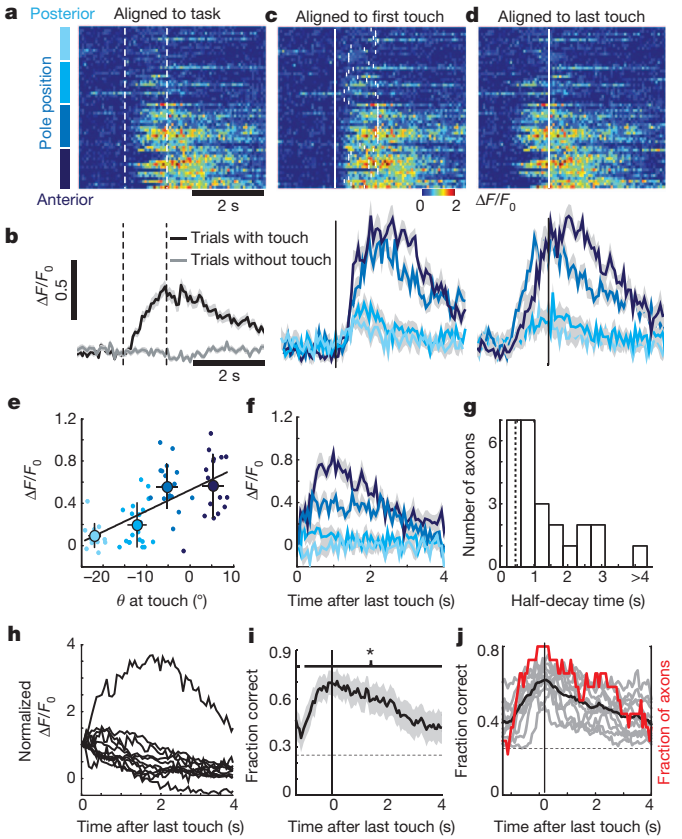

Figure 4 | Persistent object-location-dependent activity. **a**, Activity of an example axon for different object locations (hues of blue on the left; compare with Fig. 1b; only correct go trials are shown). Activity was aligned to the start of the trial (vertical dashed lines indicate presence of the pole). **b**, Activity averaged across trials with touch (black) and without touch (grey) aligned to start of trial. **c**, Same data as in **a**, aligned to the first touch (vertical line). Ticks, last touch in each trial. Bottom, activity averaged across object locations, aligned to first touch (hits). Grey shading indicates s.e.m. **d**, Same data as in **a**, aligned to the last touch. Bottom, activity averaged across object locations, aligned to last touch. **e**, Activity as a function of θ at touch. Same axon as in **a** is shown. For averaging, points were grouped by object location. Black line denotes linear regression (R^2, 0.41; $P = 2.5 \times 10^{-9}$). Error bars denote s.d. **f**, Activity averaged across object locations, aligned to the last touch and deconvolved to correct for the dynamics of calcium and GCaMP3 fluorescence (same axon as in **a**) (see Supplementary Fig. 8). **g**, Decay time of fluorescence after last touch for all axons showing object-location-dependent activity ($n = 25$). The dashed vertical line indicates $T_{1/2}$ for GCaMP3 fluorescence without persistent activity. **h**, Average fluorescence signals for axons showing persistent activity ($n = 11$). Activity was normalized to the value at the time of the last touch. **i**, The fraction of trials with correctly decoded object location as a function of time for the example axon shown in **a**–**d**. Dashed line indicates chance level (0.25, corresponding to four object locations). Horizontal line indicates time of significant decoding (*$P < 0.05$). Grey shading indicates s.e.m. **j**, Decoding of object location (same group as in **h**; black line, average; red line, fraction of axons decoding above chance level).

Axons representing different behavioural features were spatially intermingled over length scales of micrometres (Figs 2 and 3e); nearby varicosities were equally likely to be part of any of the representations. Repeated imaging experiments showed that the representations of individual axons were largely stable (Supplementary Fig. 6). The L1 apical tuft dendrites of individual neurons in vS1 may have access to a rich amalgam of contextual information.

Most of the touch-related axons showed activity that varied with object location (Fig. 3d, arrow heads; Fig. 4a–c and Supplementary Fig. 7) (25 out of 138 active axons). These axons became active only after first touch (Fig. 4a–c) (latencies greater than 100 ms) and might thus be driven in part by touch-triggered excitation spreading from vS1 to vM1 (refs 10, 11 and 13). In many cases, activation of these axons correlated with forces on a specific whisker. However, this whisker was typically not the principal whisker of the imaged barrel column (Supplementary Fig. 7). Touch-related activity corresponding to specific whiskers is thus broadcast widely to the barrel cortex, consistent with the diffuse nature of the vM1→vS1 projection[4]. These data implicate the primary motor cortex in somatosensation[26]. Furthermore, signals coding for object location are fed back from the motor cortex to the somatosensory cortex.

Fluorescence changes coding for object location often outlasted the presence of the pole, sometimes for several seconds (Fig. 4d–h and Supplementary Fig. 8). This is much longer than expected for the decay-time constant of GCaMP3 fluorescence after trains of action potentials in axons (half-decay time, $T_{1/2}$, 0.45 s; Supplementary Fig. 2) (Fig. 4g, h). After taking calcium dynamics and GCaMP3 fluorescence into account, significant graded, persistent activity was seen in 11 out of 25 object-location-sensitive axons (two-way mixed analysis of variance (ANOVA), $P < 0.05$), lasting from 0.5 s to more than 4 s (Fig. 3d, red arrowheads; Fig. 4g, h). Motor behaviours did not explain object-location-dependent persistent activity; licking and whisking were not different across trials with different object locations (two-way mixed ANOVA, 9 out of 11 persistent object location axons, $P > 0.05$; Supplementary Fig. 8f, g). Object location could be decoded from the activity of persistent axons for up to 4 s after the last contact (Fig. 4 i, j). This parametric persistent activity[26] represents a form of short-term memory of objects detected by specific whiskers at particular locations.

We used calcium imaging with genetically encoded indicators to track activity in specific projections (Fig. 1). Small patches of L1 in vS1 receive diverse signals from vM1, including activity coding for aspects of whisking, touch and licking (Figs 2 and 3). Most of the signals coded by L2/3 neurons in vM1 (ref. 12) were also represented in vM1 axons in L1 of the vS1. Touch-related and persistent activity was overrepresented in the vM1→vS1 axons, but this difference could be due to variations in the behavioural task or the sampled neuronal population.

Pyramidal neurons receive this rich top-down information in their tuft branches in L1, whereas bottom-up sensory input impinges mainly on the proximal basal dendrites[5]. L1 input increases neuronal gain and can promote bursting with coincident input in the proximal basal dendrites[27]. Pyramidal neurons therefore compare contextual input and ongoing sensory input.

Activity related to whisker position was a prominent component of the vM1→vS1 signals (Figs 2 and 3). Pyramidal neurons in vS1 might combine this efference copy-like positional information and touch input to compute object location in vS1 (refs 6 and 15). Whisking signals impinging on L1 dendrites might also selectively amplify activity related to touch during periods of active exploration.

Although mice responded within approximately 100 ms after touch in the object-localization task, a subpopulation of vM1→vS1 axons showed persistent object-location signals that outlasted the decision of

the animals by seconds (Fig. 4). These memory traces, which might not be relevant to solve this particular task, represent information about touches of specific whiskers in the recent past. Haptic object recognition is constructed from localization of several related object features, based on multiple touches over time[28,29] with multiple whiskers[30]. The vM1→vS1 projection links the past state of specific whiskers (input in L1) with present sensory input from other whiskers, ascending into vS1 through the sensory thalamus. The vS1↔vM1 loop thus has the capacity to integrate haptic information across time and space, key components of object recognition and somatosensory navigation. Pyramidal cells in vS1 receive L1 inputs related to past touch, whereas their proximal basal dendrites receive input signalling present touch. These neurons could selectively burst after specific sequences of touches with different whiskers, within time windows defined by the mnemonic activity in L1. In this scheme burst firing of populations of vS1 neurons codes for complex object shape (Supplementary Fig. 9).

METHODS SUMMARY

Virus expressing GCaMP3 (rAAV-synapsin (SYN)-GCaMP3, serotype 2/1, University of Pennsylvania Gene Therapy Program Vector Core) was injected (20 nl, 10 nl min^{-1}, 350 μm deep) into the left vM1 of adult (>P60) C57BL/6 male mice and a circular craniotomy was made over the ipsilateral vS1. Animals were trained in a whisker-dependent object-localization task. vM1 axons were imaged in the vS1 14–23 days after virus injection. Images of the whiskers were acquired using a high-speed camera at 500 frames per second. The whisker position (azimuthal angle at the whisker base, θ) and whisker shape were tracked using automated whisker tracking[8,14]. Licking was detected using an optical lickport.

Full Methods and any associated references are available in the online version of the paper.

Received 16 September 2011; accepted 12 June 2012.
Published online 26 August 2012.

1. Felleman, D. J. & Van Essen, D. C. Distributed hierarchical processing in the primate cerebral cortex. *Cereb. Cortex* **1,** 1–47 (1991).
2. Cauller, L. J. & Connors, B. W. Synaptic physiology of horizontal afferents to layer 1 in slices of rat S1 neocortex. *J. Neurosci.* **14,** 751–762 (1994).
3. Cauller, L. Layer I of primary sensory neocortex: where top-down converges upon bottom-up. *Behav. Brain Res.* **71,** 163–170 (1995).
4. Veinante, P. & Deschenes, M. Single-cell study of motor cortex projections to the barrel field in rats. *J. Comp. Neurol.* **464,** 98–103 (2003).
5. Petreanu, L., Mao, T., Sternson, S. M. & Svoboda, K. The subcellular organization of neocortical excitatory connections. *Nature* **457,** 1142–1145 (2009).
6. Hill, D. N., Curtis, J. C., Moore, J. D. & Kleinfeld, D. Primary motor cortex reports efferent control of vibrissa motion on multiple timescales. *Neuron* **72,** 344–356 (2011).
7. Knutsen, P. M., Pietr, M. & Ahissar, E. Haptic object localization in the vibrissal system: behavior and performance. *J. Neurosci.* **26,** 8451–8464 (2006).
8. O'Connor, D. H. *et al.* Vibrissa-based object localization in head-fixed mice. *J. Neurosci.* **30,** 1947–1967 (2010).
9. O'Connor, D. H., Peron, S. P., Huber, D. & Svoboda, K. Neural activity in barrel cortex underlying vibrissa-based object localization in mice. *Neuron* **67,** 1048–1061 (2010).
10. Ferezou, I. *et al.* Spatiotemporal dynamics of cortical sensorimotor integration in behaving mice. *Neuron* **56,** 907–923 (2007).
11. Kleinfeld, D., Sachdev, R. N., Merchant, L. M., Jarvis, M. R. & Ebner, F. F. Adaptive filtering of vibrissa input in motor cortex of rat. *Neuron* **34,** 1021–1034 (2002).
12. Huber, D. *et al.* Multiple dynamic representations in the motor cortex during sensorimotor learning. *Nature* **484,** 473–478 (2012).
13. Mao, T. *et al.* Long-range neuronal circuits underlying the interaction between sensory and motor cortex. *Neuron* **72,** 111–123 (2011).
14. Clack, N. G. *et al.* Automated tracking of whiskers in videos of head fixed rodents. *PLOS Comput. Biol.* **8,** e1002591 (2012).
15. Knutsen, P. M. & Ahissar, E. Orthogonal coding of object location. *Trends Neurosci.* **32,** 101–109 (2009).
16. Birdwell, J. A. *et al.* Biomechanical models for radial distance determination by the rat vibrissal system. *J. Neurophysiol.* **98,** 2439–2455 (2007).
17. Tian, L. *et al.* Imaging neural activity in worms, flies and mice with improved GCaMP calcium indicators. *Nature Methods* **6,** 875–881 (2009).
18. Trachtenberg, J. T. *et al.* Long-term *in vivo* imaging of experience-dependent synaptic plasticity in adult cortex. *Nature* **420,** 788–794 (2002).
19. Masino, S. A., Kwon, M. C., Dory, Y. & Frostig, R. D. Characterization of functional organization within rat barrel cortex using intrinsic signal optical imaging through a thinned skull. *Proc. Natl Acad. Sci. USA* **90,** 9998–10002 (1993).
20. De Paola, V. *et al.* Cell type-specific structural plasticity of axonal branches and boutons in the adult neocortex. *Neuron* **49,** 861–875 (2006).
21. Cox, C. L., Denk, W., Tank, D. W. & Svoboda, K. Action potentials reliably invade axonal arbors of rat neocortical neurons. *Proc. Natl Acad. Sci. USA* **97,** 9724–9728 (2000).
22. Hooks, B. M. *et al.* Laminar analysis of excitatory local circuits in vibrissal motor and sensory cortical areas. *PLoS Biol.* **9,** e1000572 (2011).
23. De Felipe, J., Marco, P., Fairen, A. & Jones, E. G. Inhibitory synaptogenesis in mouse somatosensory cortex. *Cereb. Cortex* **7,** 619–634 (1997).
24. Carvell, G. E., Miller, S. A. & Simons, D. J. The relationship of vibrissal motor cortex unit activity to whisking in the awake rat. *Somatosens. Mot. Res.* **13,** 115–127 (1996).
25. Komiyama, T. *et al.* Learning-related fine-scale specificity imaged in motor cortex circuits of behaving mice. *Nature* **464,** 1182–1186 (2010).
26. Hernández, A. *et al.* Decoding a perceptual decision process across cortex. *Neuron* **66,** 300–314 (2010).
27. Larkum, M. E., Senn, W. & Luscher, H. R. Top-down dendritic input increases the gain of layer 5 pyramidal neurons. *Cereb. Cortex* **14,** 1059–1070 (2004).
28. Anjum, F., Turni, H., Mulder, P. G., van der Burg, J. & Brecht, M. Tactile guidance of prey capture in Etruscan shrews. *Proc. Natl Acad. Sci. USA* **103,** 16544–16549 (2006).
29. Davidson, P. W. Haptic judgments of curvature by blind and sighted humans. *J. Exp. Psychol.* **93,** 43–55 (1972).
30. Krupa, D. J., Matell, M. S., Brisben, A. J., Oliveira, L. M. & Nicolelis, M. A. Behavioral properties of the trigeminal somatosensory system in rats performing whisker-dependent tactile discriminations. *J. Neurosci.* **21,** 5752–5763 (2001).

Supplementary Information is linked to the online version of the paper at www.nature.com/nature.

Acknowledgements We thank M. Hooks, N. Li, Z. Guo, J. Magee and J. Dudman for comments on the manuscript, N. Clack, V. Iyer and J. Vogelstein for help with software and D. Flickinger for help with microscope design.

Author Contributions L.P. and K.S. conceived the study. L.P. performed the experiments. L.P., D.A.G. and K.S. analysed the data. D.A.G. and D.H.O. contributed software. D.H. and D.H.O. helped with behavioural and imaging experiments. N.-l.X. performed key pilot studies. L.T. and L.L. provided reagents. L.P., D.A.G. and K.S. wrote the paper with comments from all authors.

Author Information Reprints and permissions information is available at www.nature.com/reprints. The authors declare no competing financial interests. Readers are welcome to comment on the online version of this article at www.nature.com/nature. Correspondence and requests for materials should be addressed to K.S. (svobodak@janelia.hhmi.org).

METHODS

Virus injection and chronic-window preparation. All procedures were approved by the Janelia Farm Research Campus Institutional Animal Care and Use Committee. Surgeries were conducted on adult (>P60) male C57BL/6 mice under isoflurane anaesthesia (1.5–2%). Other drugs reduced potential inflammation (Ketofen, 5 mg kg^{-1}, subcutaneously) and provided local (Marcaine, 0.5%, injected under the scalp) and general analgesia (buprenorphine, 0.1 mg kg^{-1}, intraperitoneally). To label motor cortex axons a small craniotomy was performed over the left vM1 (coordinates relative to bregma, anterior, 1.3 mm; lateral, 0.7 mm). Virus expressing GCaMP3 (rAAV-synapsin(SYN)-GCaMP3, serotype 2/1, University of Pennsylvania Gene Therapy Program Vector Core) was injected (20 nl, 10 nl min^{-1}, 350 µm deep) with a custom-made volumetric injection system (based on a Narishige MO-10 manipulator)[5]. Glass pipettes (Drummond) were pulled and bevelled to a sharp tip (30 µm outer diameter). Pipettes were back-filled with mineral oil and front-loaded with viral suspension immediately before injection. Compared to synthetic calcium indicators, expression of protein sensors ensures labelling of long-range axons and also allows imaging in trained mice across multiple behavioural sessions, separated by days to weeks. The virus infected neurons in layers 2–5, including most vS1-projecting neurons[13] (Supplementary Fig. 2a). A custom-machined titanium frame was cemented to the skull with dental acrylic (Lang Dental).

For imaging, a circular craniotomy was made over the left barrel cortex (vS1; diameter, 1.5 mm; centre relative to bregma, lateral, 3.5 mm; anterior, −1.4 mm; left hemisphere, Fig. 1d). An imaging window was constructed from two layers of standard microscope coverglass (Fisher; thickness, 170–210 µm), joined with an ultraviolet curable optical glue (NOR-61, Norland). A larger piece was attached to the bone and a smaller insert fit snugly into the craniotomy. The bone surrounding the craniotomy was thinned to allow for a flush fit between the insert and underlying dura. The window was cemented in place using dental acrylic (Lang Dental). After 3 days of recovery the C-row whiskers were mapped using intrinsic signal imaging[9] (Fig. 1d). Mice were anaesthetized with isoflurane (1%) after injection of chlorprothixene (1 mg kg^{-1})[31]. Images were acquired through a cranial window through a Leica MZ12.5 microscope under 630 nm illumination. Images of the vasculature over the same field of view were taken under 530 nm light-emitting diode illumination. Individual whiskers were moved using a piezoelectric bimorph (0.75 mm, 3 mm from the base; 10 Hz; 4 s, repeated every 20 s; total time, 10–30 min). Acquisition was performed with Ephus (http://www.ephus.org)[32]. Water restriction was started 1 day later.

Behaviour. The behavioural task was modified from previous studies[8,12] (Fig. 1a, b and Supplementary Fig. 1). Behavioural training began after the mice had restricted access to water for at least 7 days (1 ml per day). In the initial session mice first learned to lick for water rewards (~40 rewards). Animals were then trained to lick only in trials in which a metal pole was within easy reach of the whiskers on the right side of their face. The pole was mounted on a pneumatic linear slider (Festo; SLS-10-30-P-A Mini slide; P/N 170496) and was moved rapidly (~0.25 s) in and out of reach of the whiskers under computer control. The pole was within reach of the whiskers for ~1 s (sampling period). Tongue movements were tracked using an optical lickport.

Because the pole was placed in one of five randomly selected locations, it was impossible for mice to position their whiskers to solve the task with passive whisker stimulation. However, consistent with previous studies[8], mice tended to focus their whisking on the rewarded target locations. Passive stimulation by the moving pole thus occurred in some trials (23% of trials; 6 sessions, 5 animals). In general, mice whisked to contact the pole, but whisking varied across trials (Fig. 2b, c and Supplementary Fig. 1). Whisking strategies also varied across mice. After removal of the pole, during an answer period lasting ~1.5 s, licking was rewarded with a drop of water in go trials and punished with an extra inter-trial interval of 4 s in no-go trials. Licking was ignored in other behavioural epochs. Multiple pole positions in go trials were introduced at this early training stage. The range of go positions was initially relatively small (4.5 mm) and was gradually increased with training. The pole positions were (relative to the C2 follicle at rest) (Supplementary Fig. 1b): lateral, 6.7–9.1 mm. Go positions, centre of anterior–posterior range, 0.35–3.32 mm; anterior–posterior range, 5.6–7.0 mm; no-go positions, anterior–posterior location, 8.9–13.6 mm; lateral, 6.7–9.1 mm. Although all pole locations were within reach of the long posterior whiskers (C1, C2), mice did not always touch the most anterior (no-go) location[8] (Supplementary Fig. 1e).

Once the animals were trained ($d' > 1$), all whiskers apart from C row were trimmed on the right side of the face. Subsequent behavioural sessions were performed while imaging under the two-photon microscope.

Imaging. Imaging was performed 14–23 days after virus injection with a custom-made microscope (design available at http://research.janelia.org/Svoboda/). GCaMP3 was excited using a Ti:sapphire laser (Mai Tai, Spectra Physics) tuned to $\lambda = 925$ nm. We used GaAsP photomultiplier tubes (10770PB-40, Hamamatsu) and a ×16 (0.8 NA) microscope objective (Nikon). The field of view was 40 × 40 µm (128 × 256 pixels) (Fig. 1f), imaged at 16 Hz. The microscope was controlled with ScanImage[33] (http://www.scanimage.org). The average power for imaging was <50 mW, measured at the entrance pupil of the objective. For each mouse the optical axis was adjusted to be perpendicular to the imaging window. Imaging was stopped during inter-trial intervals (3 s; 7 s after false-alarms trials). Bleaching of GCaMP3 was negligible. Slow drifts of the field of view were corrected manually approximately every 50 trials using a reference image. In some cases we imaged the same axons over several days (Supplementary Fig. 6). Vascular landmarks and visual comparison with reference images from previous days were used to identify the same axons.

Calcium imaging has some drawbacks. Presently used genetically encoded indicators are not sufficiently sensitive to detect single action potentials, and as a consequence axons with low firing rates were probably missed[9,17] (Supplementary Fig. 2). This implies that the representations in vM1→vS1 axons are probably even richer than suggested by our imaging data. In addition, the slow dynamics (hundreds of milliseconds) of the calcium indicator limits the temporal resolution of the neurophysiological measurements. Advances in the development of fluorescent sensors of neuronal function will probably ameliorate these problems.

Image analysis. Frames were registered using rigid translation based on cross-correlation[34]. First, we selected a trial with little movement and the frames within the trial were registered and averaged. All of the frames from a session were registered to this averaged image. To extract fluorescence signals, ROIs were drawn over fluorescent varicosities identified by using the mean, maximum intensity and standard deviation values of all trials. The pixels in each ROI were averaged to estimate fluorescence corresponding to a single varicosity. The baseline fluorescence of the ROI, F_0, was estimated as the 30th percentile of the fluorescence using a 32 s sliding window and used to calculate $\Delta F/F_0 = ((F - F_0)/F_0)$. To produce an event vector from the $\Delta F/F_0$ trace, and thereby minimize the temporal distortions caused by GCaMP3 dynamics[17], we used a non-negative deconvolution method[35]. These event vectors were used to train the decoder and to measure average activity when selecting for active axons. Active axons were defined as having an average event rate higher than 0.007 events per frame and a peak $\Delta F/F_0$ in the peristimulus time histograms higher than 30% for any trial type (that is, hit, correct rejection or false alarm). This assures that the calcium signals are not due to motion artefacts (less than 1% of the GCaMP3 signals are expected to be polluted by movement) (Supplementary Fig. 3).

Whisker tracking. Whiskers were illuminated using a high-power light-emitting diode (940 nm, Roithner) and condenser optics (Thorlabs). Images were acquired through a telecentric lens (×0.36, Edmund Optics) by a high-speed CMOS camera (EoSense CL, Mikrotron) running at 500 frames per second (640 × 352 pixels; 42 pixels per mm). Image acquisition was controlled by Streampix 3 (Norpix, Canada). The whisker position (θ) and whisker shape were tracked using automated whisker tracking[8,14] (https://openwiki.janelia.org/wiki/display/MyersLab/Whisker+Tracking). Whiskers are cantilevered beams, with one end embedded into the follicle in the whisker pad. Measurement of whisker shape and the mechanical properties of the whisker can be used to estimate the forces acting on the follicle[16]. The amplitudes of the forces in the follicle are proportional to the curvature change of the whisker, $\Delta\kappa$. We used $\Delta\kappa$ at a particular location along the whisker (2–3 mm) as a substitute for the mechanical forces acting on the whiskers[14,16]. Curvature was measured from a parametric curve comprising second-order polynomials fitted to the whisker backbone. Periods of contact between the whisker and object (touch) were detected on the basis of nearest distance between whisker and object.

Behavioural features. Licking was detected using a lickometer[8]. Lick rate (Hz) was the inverse of the inter-lick interval. Motor cortex neurons primarily code for slow variables related to whisking[6,24]. We decomposed whisking (that is, θ at base) into whisking set-point and whisking amplitude. Whisking set-point was defined as the 0.6 s moving average of θ. Whisker amplitude was defined as the Hilbert transform[36] of the absolute value of the band-pass filtered (6–30 Hz) θ. Whisking set-point and whisker amplitude were highly correlated in our behavioural task (Supplementary Fig. 5a) and only one of these features (whisking amplitude) is shown in most figures (Figs 2 and 3). To characterize the quality of the decomposition we reconstructed whisker position from set-point, whisker amplitude and whisking phase. The reconstruction error (root mean squared error) across all animals was 4.5 ± 0.18° (mean ± s.e.m.; range 3.5–6.1°), corresponding to 30% of the variance of whisker position. The analysis of curvature was restricted to periods of touch. We further derived features related to protraction touch (negative $\Delta\kappa$) and retraction touch (positive $\Delta\kappa$) and separately absolute values.

All behavioural features were down-sampled to the image-acquisition rate (16 Hz). Mean and maximum values were calculated for each feature in a 64-ms window centred on the middle of the new sampling point. Mice whisk at frequencies above 8 Hz (the Nyquist frequency)[37] and this information is lost by

down-sampling. Across animals, 48 ± 1% of the energy of the whisking trajectory was contained at frequencies below 8 Hz. The higher frequency signals (that is, phase) are not thought to be coded by most of the motor cortex neurons[6,24]. Also, our imaging methods would be too slow to capture modulation with whisking phase.

Correlation analysis to determine if multiple varicosities are part of the same axon. vM1 axons form elaborate arborizations in L1 of the vS1, and multiple varicosities in one field of view were often part of the same axon. To characterize the diversity of signals impinging on vS1, we wanted to report activity in distinct axons, as opposed to distinct varicosities. We used correlation-based methods to distinguish varicosities that were part of the same axon and those that were part of different axons (Fig. 1h–j).

We first selected varicosities that, on the basis of structural images, were part of the same axon (14 sessions). We computed their correlation coefficient over an entire session, and compared them to correlation coefficients computed over all pairs of varicosities (dominated by pairs from different axons). As expected[21,38], pairs of varicosities from the same axon showed markedly higher correlation coefficients compared with random pairs. The correlation coefficient increases with increasing event rates. For varicosities from the same axon we plotted the correlation coefficients as a function of event rates and fitted an exponential curve to the data (Fig. 1j). The 95% confidence value of the fit was used as a criterion to assign pairs of varicosities to the same axon, even in the cases where the axonal morphology could not be discerned.

To build clusters of correlated ROIs we selected all the pairs that were considered to be from the same axon on the basis of correlations (Fig. 1h–j). We seeded a cluster with one randomly selected pair. The next randomly selected pair could share one of the ROIs with the existing cluster, in which case it joined the cluster; otherwise it seeded a second cluster, and so on. We iterated this procedure until all pairs were assigned. Each cluster was represented in the data set by a 'representative' ROI, defined by the largest mean $\Delta F/F_0$.

Characterizing movement using mice with GFP-expressing axons. Axons and their varicosities are tiny structures (one micrometer diameter, or less[20]). Movement of the animal could displace axons in and out of the objective focal plane and thus produce motion artefacts in the fluorescence signal. To quantify these errors we performed control experiments in three mice with vM1→vS1 axons labelled with green fluorescent protein (GFP). All experimental conditions were identical, except that rAAV-SYN-GFP (serotype 2/1) was injected into vM1 instead of the GCaMP3-expressing virus. These mice were trained in the object-localization behaviour and analysed identically to mice expressing GCaMP3 (Supplementary Fig. 3). Although varicosities in GFP animals showed movement-induced changes in fluorescence, mainly during the licking period, these changes rarely exceeded 25%.

Characterization of axonal varicosities in brain slices. Male C57BL/6 mice (P15) were injected in the left vM1 with 20 nl AAV-SYN-GCamP3, serotype 2/1 as described[5]. Two weeks later vS1 slices were prepared. Mice were anaesthetized with an intraperitoneal injection of a ketamine/xylazine mixture (0.13 mg ketamine and 0.01 mg xylazine per gram of body weight) and perfused through the heart with ice-cold artificial cerebrospinal fluid (ACSF; ~5 ml) containing 127 mM NaCl, 25 mM $NaHCO_3$, 25 mM D-glucose, 2.5 mM KCl, 1 mM $MgCl_2$, 2 mM $CaCl_2$ and 1.25 mM NaH_2PO_4, aerated with 95% O_2 and 5% CO_2. The brain was removed and placed into ice-cold cutting solution containing 110 mM choline chloride, 25 mM $NaHCO_3$, 25 mM D-glucose, 11.6 mM sodium ascorbate, 7 mM $MgCl_2$, 3.1 mM sodium pyruvate, 2.5 mM KCl, 1.25 mM NaH_2PO_4 and 0.5 mM $CaCl_2$. Coronal slices (300 μm thick) of the right barrel cortex were cut with a vibrating slicer (Microm, Walldorf) and incubated in oxygenated ACSF for 45 min at 37 °C and then at room temperature (approximately 23 °C). For recording, slices were placed in a chamber with circulating ACSF at 34 °C under a custom-built two-photon microscope. A 40 × 40 μm area of L1 in the barrel cortex was imaged at 16 Hz using a Ti:sapphire laser tuned to $\lambda = 925$ nm. L1 axons were stimulated with an extracellular electrode at 83 Hz. Fluorescence traces were extracted as described for the *in vivo* experiments.

Decoding behavioural variables. The relationship between fluorescence signal x_i of the ith axon and the jth behavioural variable y_j can be characterized as an encoding description $P(x_i|y_j)$ or a decoding description $P(y_j|x_i)$. The encoding description specifies how much of the activity of the axon can be accounted for by the behavioural variables. The decoding description specifies how well a behavioural variable can be derived from the activity of populations of axons (Fig. 3a and Supplementary Fig. 4) or single axons (Figs 3b–e and 4i, j). Here, we focused on the decoding description.

We used machine learning algorithms to decode the behavioural variables based on activity. For single axon decoding (Fig. 3b–e) each axon was used to predict behavioural variables, such as forces on each whisker, whisking amplitude and lick rate. The input to the algorithm was the event rate (that is, deconvoluted $\Delta F/F_0$) of a given axon as well as time-shifted versions. To predict sensory input we used present and future activity. For motor variables we used both past and future values, as neural activity could reflect motor commands, corollary discharges or re-afferent input.

The goal of the decoder algorithm was to find a mapping $\hat{y}_j(t_k) = f[x_i(t_{k-l}), \ldots, x_i(t_k), \ldots, x_i(t_{k+p})]$ that best approximates $y_j(t_k)$ for all t_k. t_k is discretized time (in units of 1/16 s, corresponding to the imaging rate); l and p represent the maximum negative and positive shifts of the activity, respectively.

We concatenated trials to generate a vector $\bar{t}$ of time-binned data. For sensory variables we used $l = 5$ and $p = 0$ and for sensory–motor variables $l = 5$ and $p = 5$ (corresponding to time-shifts up to 0.32 s). The dimensionality of the input variables is $l + p + 1$.

For decoding neural populations (Fig. 3a and Supplementary Fig. 4a) we used for each session all axons showing at least one event and created an input vector of size $N_{\text{axons}} \times (l + p + 1)$. Each behavioural session, corresponding to one imaged field of view, was treated separately.

The algorithm was trained on a subset of trials (the training set, 80%) and evaluated on a separate set of test trials (20%) We repeated this procedure five times to obtain a prediction for all trials[39].

The accuracy of the decoding algorithm was evaluated using the Pearson correlation coefficient (ρ) between the model estimate and the data. The explained variance is $R^2 = \rho^2$ (range, 0–1). R^2 was calculated separately for each trial type (that is, hit, correct rejection, miss and false alarm). Treating trial types separately was critical to disambiguate the relationship between different behavioural variables and activity of single axons. For instance, we observed large-amplitude whisking during licking, which complicates the classification of the response type of the axon. However, during correct-rejection trials, licking was absent and whisking present, simplifying the classification of axon types. Similarly, in trained animals, touch and licking occurred with short latencies in hit trials. By contrast, in false-alarm trials touch was typically absent or diminished in magnitude.

Decoding was with Random Forests[39,40], a multivariate nonparametric machine learning algorithm based on bootstrap aggregation (that is, bagging) of regression trees. We used the TreeBagger class implemented in Matlab. TreeBagger requires only few parameters: the number of trees ($N_{\text{trees}} = 32$), the minimum leaf size (minleaf = 10), the number of features chosen randomly at each split ($N_{\text{split}} = N_{\text{features}}/3$; the typical value used by default[40]). These parameters were chosen as a trade-off between decoder accuracy and computation time. We did not observe much improvement in decoding accuracy for $N_{\text{trees}} > 32$ and minleaf < 10 (data not shown).

Classification of response types. We measured the R^2 between each measured behavioural variable (that is, whisking amplitude, lick rate, whisking set-point, etc) and each axon's decoder prediction for all the trials and for each trial type (Fig. 3b–e). In addition, we used ANOVA to determine whether calcium responses were different for different pole locations (Fig. 4). We grouped the behavioural variables in larger categories such as whisking (that is, including whisking amplitude and whisker set-point), lick rate and touch (that is, touch per whisker, rate of change of forces, absolute magnitude, etc). We considered the best R^2 set for each of the three behavioural categories. Alternatively, all axons were classified manually on the basis of trial-to-trial calcium transients and behavioural prediction for each trial type. For most axons classification was unambiguous based on the decoder R^2 values. The remaining axons were more accurately classified based on a rarer trial type. For example, touch-related axons were much more active in trials with touches compared to trials without touches (Supplementary Fig. 4c). Lick-related axons, but not touch-related axons, were active during licking in false-alarm trials. Three of the authors independently arrived at consistent classifications.

Clustering of response types. We used clustering algorithms to display the trial-averaged responses of all active unique axons (Fig. 3b). First, we divided the axons into five categories: touch, whisking, licking, mixed and unclassified. Within each category we computed a similarity index between pairs of axons based on the trial-averaged responses in hit, correct-rejection and false-alarm trials. For each axon we concatenated their trial-averaged response for these three trial types. The similarity index was the pairwise correlation between the concatenated trial-average responses between every axonal pair. We computed a weighted correlation to take into account that the number of false-alarm trials is typically lower than either hit or correct-rejection trials.

Given the two vectors $\bar{y}$ and $\bar{x}$ and the weight vector $\bar{w}$ (by the relative number of trials in each trial type):

$$\text{Weighted mean: } \mu(\bar{x};\bar{w}) = \frac{\sum_i w_i x_i}{\sum_i w_i}$$

$$\text{Weighted covariance: } \operatorname{cov}(\bar{x},\bar{y};\bar{w}) = \frac{\sum_i w_i (x_i - \mu(\bar{x};\bar{w}))(y_i - \mu(\bar{y};\bar{w}))}{\sum_i w_i}$$

$$\text{Weighted correlation: } \operatorname{corr}(\bar{x},\bar{y};\bar{w}) = \frac{\operatorname{cov}(\bar{x},\bar{y};\bar{w})}{\sqrt{\operatorname{cov}(\bar{x},\bar{x};\bar{w})\operatorname{cov}(\bar{y},\bar{y};\bar{w})}}$$

Axons were reordered using hierarchical clustering for each category separately (using linkage and dendrogram from Matlab with unweighted average distances between clusters).

Analysis of sustained activity. For all cells showing object-location-dependent activity we tested for parametric persistent activity. Fluorescence traces were deconvolved with an exponential decay characterized by the GCaMP3 decay-time constant ($T_{1/2} = 0.45$ s) (compare Fig. 4d, f and Supplementary Fig. 8c, d). The mean value of the deconvolved traces at different times after contact (0.2–1.1, 1.1–2.0, 2.0–2.9 and 2.9–3.8 s after the last contact) was tested for object-location-dependent activity (two-way mixed-effect ANOVA). To determine whether object-location-dependent motor behaviours could explain object-location-dependent activity, similar analyses were performed for lick rate and whisking parameters (Supplementary Fig. 8f, g).

We applied linear and nonlinear decoders (Random Forests, linear and quadratic discriminant analysis; naive Bayes was also tested and gave identical results to linear discriminant analysis) to determine the time course of the object-location memory traces and compared their performance (Supplementary Fig. 8h). Each decoder was trained to predict the pole position as a function of time on the basis of the average activity (that is, events) in the previous 0.5 s for each axon. We performed 200 repetitions of this procedure to compute the average performance of each decoder and their confidence intervals. We ensured that there was an equal number of trials per each of the four possible pole positions (that is, chance level corresponded to 0.25). As before, we used 80% of the trials to train the decoders and tested the performance in the remaining 20% trials (repeating this five times to obtain a prediction for the full set of trials). The linear and quadratic discriminant decoders assume that the input is a multivariate Gaussian and find the optimal linear or quadratic curve that best separates the classes[41].

31. Kaneko, M., Hanover, J. L., England, P. M. & Stryker, M. P. TrkB kinase is required for recovery, but not loss, of cortical responses following monocular deprivation. *Nature Neurosci.* **11,** 497–504 (2008).
32. Suter, B. A. *et al.* Ephus: multipurpose data acquisition software for neuroscience experiments. *Front. Neural Circuits* **4,** 100 (2010).
33. Pologruto, T. A., Sabatini, B. L. & Svoboda, K. ScanImage: flexible software for operating laser-scanning microscopes. *Biomed. Eng. Online* **2,** 13 (2003).
34. Guizar-Sicairos, M., Thurman, S. T. & Fienup, J. R. Efficient subpixel image registration algorithms. *Opt. Lett.* **33,** 156–158 (2008).
35. Vogelstein, J. T. *et al.* Fast nonnegative deconvolution for spike train inference from population calcium imaging. *J. Neurophysiol.* **104,** 3691–3704 (2010).
36. Hill, D. N., Bermejo, R., Zeigler, H. P. & Kleinfeld, D. Biomechanics of the vibrissa motor plant in rat: rhythmic whisking consists of triphasic neuromuscular activity. *J. Neurosci.* **28,** 3438–3455 (2008).
37. Voigts, J., Sakmann, B. & Celikel, T. Unsupervised whisker tracking in unrestrained behaving animals. *J. Neurophysiol.* **100,** 504–515 (2008).
38. Koester, H. J. & Sakmann, B. Calcium dynamics associated with action potentials in single nerve terminals of pyramidal cells in layer 2/3 of the young rat neocortex. *J. Physiol.* **529,** 625–646 (2000).
39. Hastie, T., Tibshirani, R. & Friedman, J. *The Elements of Statistical Learning* 2nd edn (Springer, 2009).
40. Breiman, L. Random forests. *Mach. Learn.* **45,** 5–32 (2001).
41. Duda, R. O., Hart, P. E. & Stork, D. G. *Pattern Classification* 2nd edn (Wiley, 2001).